iScience

Article

Unsupervised spatiotemporal classification of deformation patterns of embryonic tissues matches their fate map

Graphical abstract

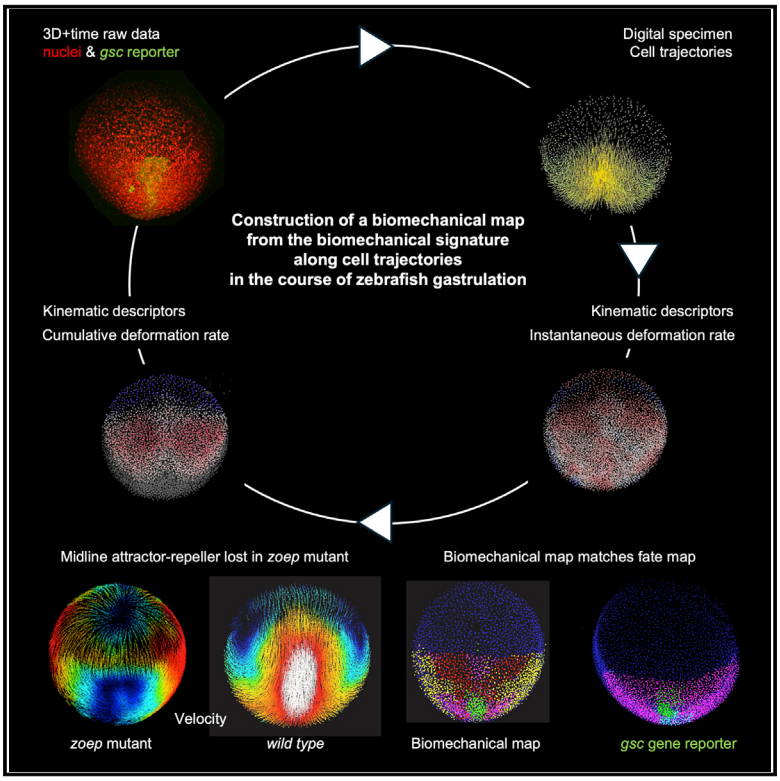

Authors

David Pastor-Escuredo,
Benoît Lombardot, Thierry Savy, ...,
Juan C. del Álamo,
María J. Ledesma- Carbayo,
Nadine Peyriéras

Correspondence

david@lifedlab.org (D.P.-E.),
mj.ledesma@upm.es (M.J.L.C.),
nadine.peyrieras@cnrs.fr (N.P.)

In brief

Biological Sciences; Developmental biology; Complex Sytems; Biological constraints; Model organism

Highlights

- Kinematics descriptors provide precise and robust developmental landmarks
- Cumulative deformation rates during gastrulation compensate for local fluctuations
- Individual cells and morphogenetic fields have a biomechanical signature
- Cells' biomechanical signature matches their fate and marker's expression
- Midline plays the role of an attractor-repeller lost in zoep mutants

Pastor-Escuredo et al., 2025, iScience *28*, 111753
March 21, 2025
https://doi.org/10.1016/j.isci.2025.111753

CellPress

iScience

CellPress
OPEN ACCESS

Article

Unsupervised spatiotemporal classification of deformation patterns of embryonic tissues matches their fate map

David Pastor-Escuredo,[1,2,3,11,*] Benoît Lombardot,[4] Thierry Savy,[1,4,9] Adeline Boyreau,[1] René Doursat,[1,4] Jose M. Goicolea,[5] Andrés Santos,[2,3] Paul Bourgine,[1,4,9] Juan C. del Álamo,[6,7,8,10] María J. Ledesma- Carbayo,[2,3,10,*] and Nadine Peyriéras[1,4,9,10,*]

[1]USR3695/FRE2039 BioEmergences, CNRS, Paris-Saclay University, Gif-sur-Yvette, France
[2]Biomedical Image Technologies, ETSIT, Universidad Politécnica de Madrid, 28040 Madrid, Spain
[3]Biomedical Research Center in Bioengineering, Biomaterials and Nanomedicine (CIBER-BBN), Instituto de Salud Carlos III, Madrid, Spain
[4]UPS3611 Complex Systems Institute Paris Ile-de-France (ISC-PIF), CNRS, Paris, France
[5]Computational Mechanics Group, Universidad Politécnica de Madrid, 28040 Madrid, Spain
[6]Mechanical and Aerospace Engineering Department, University of California San Diego, La Jolla, CA 92093, USA
[7]Mechanical Engineering Department, University of Washington, Seattle, WA 98195, USA
[8]Center for Cardiovascular Biology, University of Washington, Seattle, WA 98109, USA
[9]Matières et Systèmes Complexes (MSC) UMR7057, CNRS, Université Paris Cité, 10 rue Alice Domon et Léonie Duquet, 75013 Paris, France
[10]These authors contributed equally
[11]Lead contact
*Correspondence: david@lifedlab.org (D.P.-E.), mj.ledesma@upm.es (M.J.L.C.), nadine.peyrieras@cnrs.fr (N.P.)
https://doi.org/10.1016/j.isci.2025.111753

SUMMARY

During morphogenesis, embryonic tissues display fluid-like behavior with fluctuating strain rates. Digital cell lineages reconstructed from 4D images of developing zebrafish embryos are used to infer representative tissue deformation patterns and their association with developmental events. Finite deformation analysis along cell trajectories and unsupervised machine learning are applied to obtain reduced-order models condensing the collective cell motions, delineating tissue domains with distinct 4D biomechanical behavior. This reduced-order kinematic description is reproducible across specimens and matches fate maps of the zebrafish brain in wild-type and nodal pathway mutants (*zoep*$^{tz57/tz57}$), shedding light into the morphogenetic defects causing these mutants' cyclopia. Furthermore, the inferred kinematic maps also match expression maps of the gene transcription factor *goosecoid* (*gsc*). In summary, this work introduces an objective analytical framework to systematically unravel the complex spatiotemporal patterns of embryonic tissue deformations and couple them with cell fate and gene expression maps.

INTRODUCTION

Embryonic morphogenesis depends on the mechanical properties of the cells making up tissues, in conjunction with the generation and transduction of forces controlling their interactions.[1,2] Mechanical stimuli affect all levels of biological organization, including gene expression and the signaling activities that underlie cell proliferation and cell death.[3,4] The robustness of embryonic development relies on coordinating these processes in space and time.[5–8] Time-lapse microscopy has made it possible to trace cell lineages in live developing embryos,[9–16] paving the way to quantifying tissue kinematics during morphogenesis.[17,18] Previous studies in two dimensions have shown that specific mutations affect tissue kinematics.[18–20] Furthermore, mathematical models of tissue biomechanics representing collective cell interactions can quantify the mechanical forces involved in morphogenesis in two[21–25] and three dimensions.[26] However, extracting the representative 4D (three-dimensional and time-resolved - 3D + time) features of tissue kinematics and linking these features to gene expression and cell fate[27–29] is challenging.[30,31]

Because its embryos develop rapidly and are transparent, zebrafish is the vertebrate model of choice to investigate the spatiotemporal tissue kinematics during gastrulation.[32–34] Starting from the velocity fields obtained from digital cell lineages,[35,36] we quantify tissue deformation, including compression or expansion, distortion, and rotation. Incremental deformations at the lengthscale of a cell fluctuate both in space and time and vary among specimens. However, these fluctuations are cumulatively balanced along cell trajectories leading to reproducible time courses of overall deformation along gastrulation. We exploit this finding and combine unsupervised machine learning with 4D cell tracking to cluster cell populations according to the similarity of the deformation time courses along their trajectories.[37,38] This analysis yields a surprisingly low number of clusters that show spatial coherence, match

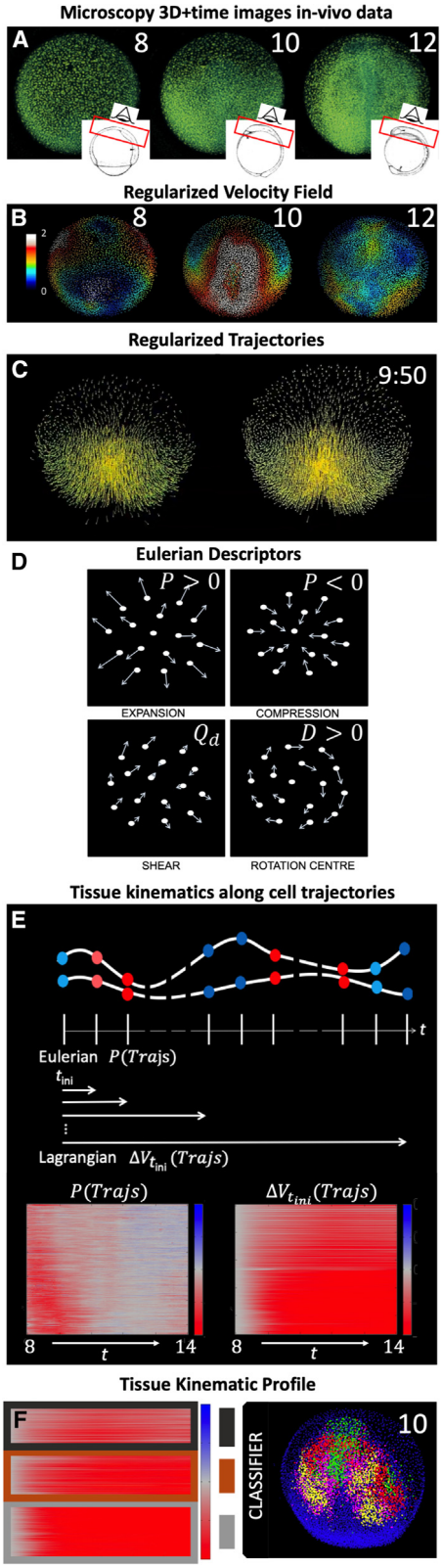

morphological landmarks and gene expression patterns, and facilitate the interpretation of collective cell motions and tissue deformations. Differences observed between wild-type and mutant embryos (*zoep*$^{tz57/tz57}$, deficient for the transduction of the Nodal pathway[39]) showed that in mutants, altered deformation patterns are associated with the cyclopic phenotype. Overall, we introduce a conceptual and analytical framework to unravel the complex spatiotemporal patterns of embryonic tissue deformations and relate them to cell fate and gene expression maps.

RESULTS

Eulerian tissue deformation provides landmarks of morphogenetic transitions in zebrafish early embryogenesis

We quantified mechanical strains at the tissue scale based on regularized cell lineage trees reconstructed from 4D imaging data of zebrafish embryos developing from 6 hours post fertilization (hfp) to 14 hpf[36] at 26°C (Figures 1A–1C). Using these data, we computed tissue kinematics descriptors based on invariants of the instantaneous deformation gradient (IDG) tensor in the Eulerian reference frame, and of the finite-time deformation gradient (FTDG) tensor in the Lagrangian reference frame of each cell (Figure 1D). We then constructed maps of these descriptors along and across the developing embryo's cell trajectories (Figure 1E) and analyzed these maps to extract the most representative patterns of tissue kinematics (Figure 1F). Finally, we performed a clustering analysis to determine the cells within

Figure 1. Construction of the biomechanical map from the reconstructed cell lineage

(A–C) WT specimen *wt1* imaged live between 6 and 12 hpf, animal pole (AP) view, rendered in 3D using the Mov-IT software. Scale bar 50 μm.

(A) Nuclear staining (green) shown at 8, 10 and 12 hpf as indicated in each panel. The insets depict the imaged volume and field of view.

(B) Cell velocity magnitudes obtained from the cells' regularized displacement field (see STAR Methods, Figure S2) and represented in $\mu m/sec$ as indicated by color bar.

(C) Original cell trajectories (left panel) vs. regularized ones (right panel). Cell nuclei are shown as cubes and 5-time-step segments of their trajectories are shown by lines.

(D) Schematics of simple cell flows, associated tissue deformation patterns, and corresponding IDG descriptors: expansion ($P>0$), compression ($P<0$), shear (Q_d), and rotation ($D>0$).

(E) Schematic illustration depicting the computation of tissue kinematics descriptors along cell trajectories. Tissue deformation invariants are computed at each point along the cell trajectories from the instantaneous (Eulerian) or finite time (Lagrangian) deformation gradients (e.g., P and $\Delta V_{t_{ini}}$, respectively, where red indicates compression and blue indicates expansion blue). The resulting time-dependent profiles are plotted for a selection of cells between 8 (t_{ini}) and 14 hpf, leading to an atlas of tissue kinematics maps along cell trajectories.

(F) Overview of the two-step clustering approach used to identify embryonic domains undergoing distinct tissue kinematics. First, we cluster each map within the atlas to identify representative tissue kinematics profiles (RTKPs, dark gray, brown, light gray). Second, the RTKPs are used to classify cells within the embryo, revealing connected embryonic domains that experience distinct spatiotemporal evolution of tissue kinematics (red, magenta, green and yellow).

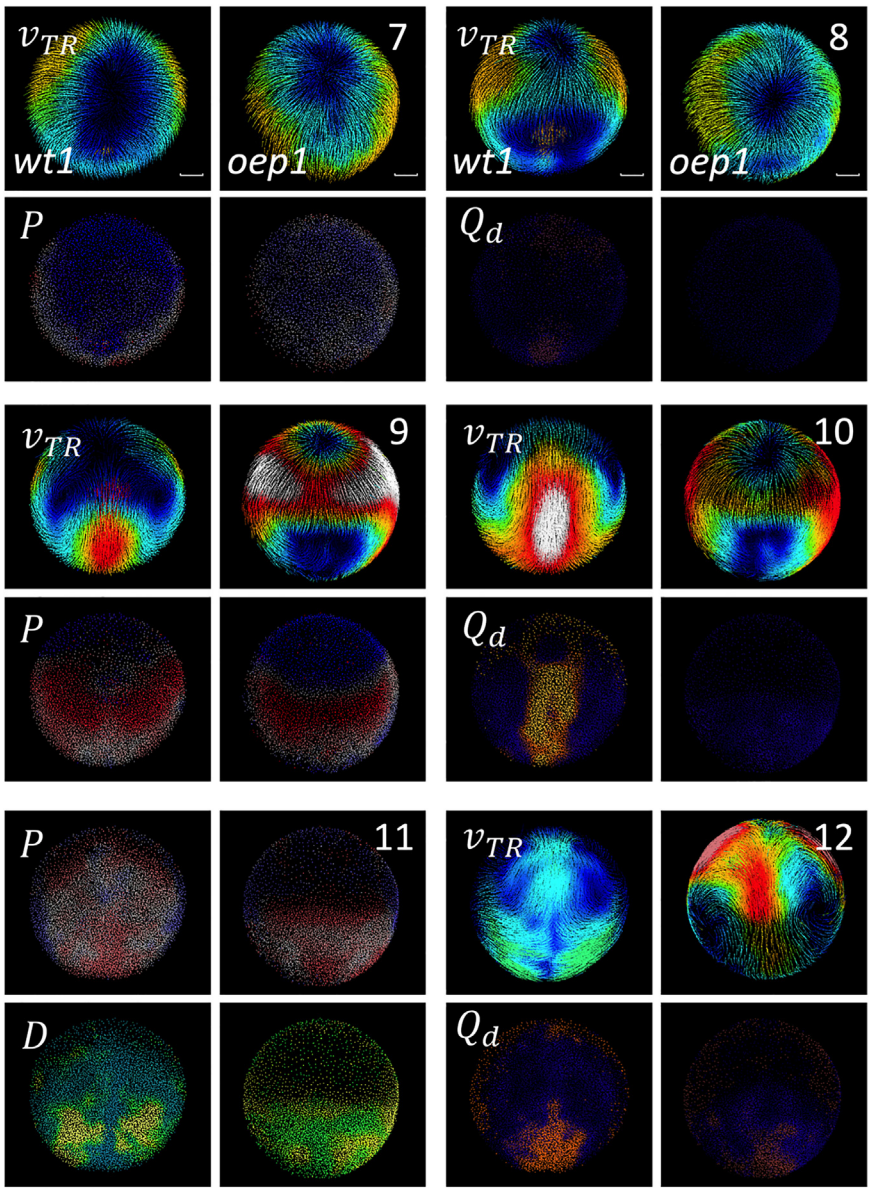

Figure 2. Biomechanical landmarks of gastrulationin *wt* and *zoep*$^{tz57/tz57}$

Comparison between a wild-type embryo *wt1* (columns 1 and 3) and a *zoep*$^{tz57/tz57}$ mutant embryo *oep1* (columns 2 and 4). Time point (7, 8, 9, 10, 11 and 12 hpf) indicated to right. Descriptor indicated top left of each pair (*wt1* and *oep1*) of panels. Velocity field (v_{TR}) colormap from dark (zero) to white (2 $\mu m/sec$). *P* colormap goes from compression (red) to neutral (gray) to expansion (blue). Q_d colormap from dark (no distortion) to bright (maximum distortion). *P* Rotation discriminant *D* colormap from blue (no rotation) to green-yellow (maximum rotation observed). Scale bar 50 μm.

For a Figure360 author presentation of Figure 2, see https://doi.org/10.1016/j.isci.2025.111753#mmc29. Figure360▷

the embryo that most closely followed each representative pattern of tissue kinematics.

This methodology was applied to six wild-type embryos (*wt1-wt5, wt6*) (Videos S1 and S2), one of them carrying a GFP reporter to monitor the expression of *goosecoid* (*gsc*) transcription factor, and five *zoep*$^{tz57/z57}$ mutants (*oep*1-*oep*5, Video S3) with a deficiency in the transduction of nodal signals that leads to cyclopia (Table S1). Embryos were imaged from the animal pole throughout gastrulation (Figures 1A and S1) to observe the development of their anterior region that includes part of the forebrain and midbrain (temporal resolution 2.5 min/frame; voxel size: 1.4 μm^3 (Video S1, Table S1)).

The tissue mechanical strains were calculated from a regularized velocity field (v_{TR}, Figures 1B and 2 first column), obtained by convolving the measured cell displacements with a 4D Gaussian kernel filter (timescale T = 10 min, lengthscale R = 20 μm). The filter's lengthscale covered one or two rows of neighboring cells depending on the developmental stage since cell size diminished throughout gastrulation (supplementary information). Cell tracking errors were corrected automatically to ensure the continuity of cell trajectories (Figure 1C). The Eulerian descriptors of tissue kinematics were determined from tissue strains by computing the incremental deformation gradient (IDG) tensor field[40,41] (Figure 1D) and, more specifically, its first invariant *P,* the second invariant of its deviatoric part,[3] Q_d, and its rotation discriminant, *D*. These invariants indicate compression or expansion, shear distortion, and circular motion caused by cell motion, cell shape changes, and cell intercalation (Figure 1D; Tables S2 and S4). These descriptors were rendered as 4D spatiotemporal maps using the visualization interface Mov-IT[36] to display the patterns of mechanical activity in the zebrafish anterior region between 6 and 14 hpf at 26°C (Videos S4, S5, S6, S7, S8, and S9).

Eulerian descriptor maps reveal morphogenetic transitions involving sharp changes in tissue kinematics. In wild-type embryos (Figure 2; Figures S3 and S5, Videos S4, S5, S6, S7, S8, S9, S11, S12, S13, S14, and S15). Epibolic planar expansion of the blastoderm over the yolk was dominant at the onset of gastrulation (6 hpf), with cells diverging from the animal pole. The *zoep*$^{tz57/tz57}$ mutant (Figure 2; Figure S4, Videos S10, S16, S17) showed a similar behavior at that early stage, but differences in tissue kinematics emerged as gastrulation proceeded (7–8 hpf). Wild-type embryos experienced rapid tissue motion, a dorsoventral expansion-compression front, and distortion of the hypoblast, a disruption pattern absent in the *zoep*$^{tz57/tz57}$ mutant. This pattern

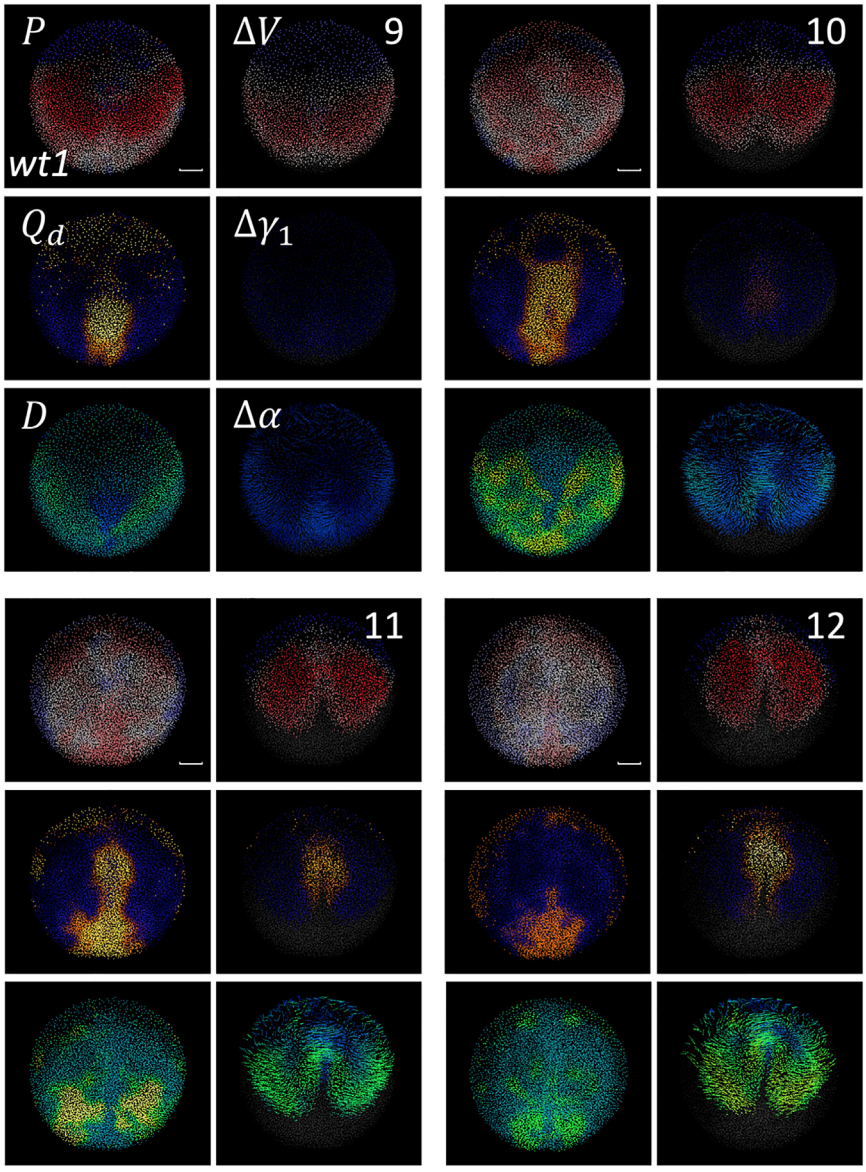

Figure 3. Cumulative descriptors of *wt* development

Comparison between Eulerian and Lagrangian descriptors for wild-type embryo *wt1* at four time points during gastrulation (9, 10, 11 and 12 hpf, as shown at the top right corner of each panel group). The deformation descriptors shown are *P*, ΔV, Q_d, $\Delta\gamma_1$, and $\Delta\alpha$ from left to right and from top to bottom, as indicated in the top left panel group. Lagrangian (ΔV, $\Delta\gamma_1$ and $\Delta\alpha$) and Eulerian (*P*, Q_d, *D*) descriptors are juxtaposed in the left and right columns of each panel group, respectively. Lagrangian descriptors use the following color schemes: ΔV colormap from compression (red) to neutral (gray) to expansion (blue); $\Delta\gamma_1$ colormap from dark (no distortion) to bright (maximum distortion); $\Delta\alpha$ colormap from blue (no rotation) to green-yellow (maximum rotation). Eulerian descriptors use the following color schemes: *P* colormap from compression (red) to neutral (gray) to expansion (blue); Q_d from dark (no distortion) to bright (maximum distortion); *D* colormap goes from blue (no rotation) to green-yellow (maximum rotation). Scale bar 50 μm.

persists and strains intensify until mid-gastrulation (8–9 hpf). It goes with strong tissue shear along the embryonic midline due to the relative motions of the hypoblast (internal) and epiblast (external) cell layers. The dorsoventral expansion-compression front eventually developed in the *zoep*$^{tz57/z57}$ mutant (9–11 hpf) but, consistent with this mutant's defect in hypoblast formation, shear between the internal and external cell layers is not observed. Concomitant with this defect, the coordinated bilateral rotational motions that form on both sides of the midline (9–12 hpf) in wild-type embryos were weaker in *zoep*$^{tz57/z57}$ mutants and failed to progress anteriorly. Consequently, tissue convergence toward the midline and antero-posterior axis elongation, reflected by a progressive increase in compression and shear along the midline in wild-type embryos, were impaired and relegated to the posterior region in the *zoep*$^{tz57/z57}$ mutant. Of note, the absence of coordinated bilateral rotation patterns in the anterior region of the mutant embryo, known to develop cyclopia, suggests that this tissue deformation is essential to split the eye field and form bilateral eyes. At the end of gastrulation and onset of neurulation (from 12 hpf), the Eulerian descriptors did not show any coherent large-scale tissue motion.

Lagrangian tissue deformation along cell trajectories robustly captures 4D tissue mechanics during zebrafish early embryogenesis

The Eulerian descriptors of tissue kinematics exhibited fluctuations in space and time, as well as variation between different specimens (see, e.g., Videos S4, S5, S6, S7, S8, and S9). This variability contrasts with the persistence of the fate map patterns, suggesting that spatiotemporal fluctuations are compensated so that the cumulative deformations along cell trajectories are stable. Consequently, we determined Lagrangian descriptors of tissue deformation following each cell's trajectory during development. These descriptors are invariants of the FTDG, which, in contrast to its instantaneous counterpart, measures cumulative deformation from a reference instant of time t_{ini}. Specifically, we determined Lagrangian volume change, rotation angle, and tissue distortions (ΔV, $\Delta\alpha$, and $\Delta\gamma_1$ and $\Delta\gamma_2$ respectively, see Tables S3 and S4).

Figure 3 displays Lagrangian descriptors of tissue kinematics for a wild-type embryo using t_{ini} between 7 and 8 hpf (time window that depends on slight development temperature difference between the specimens) as reference state (see also Figure S6; Video S19 and S20). In the same figure, analogous Eulerian descriptors are displayed side by side for comparison (e.g.,

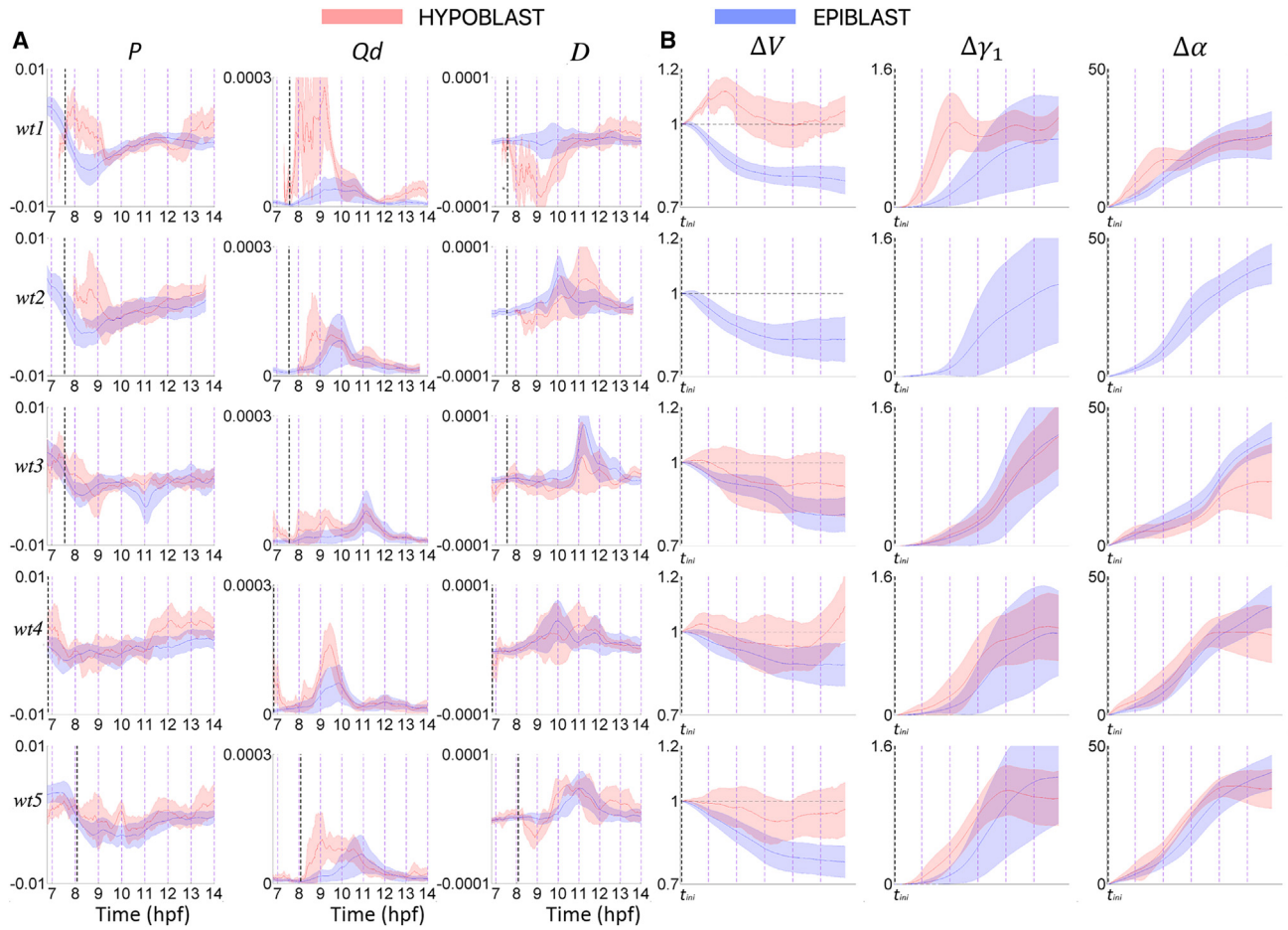

Figure 4. Quantitative comparison of Lagrangian Kinematic Profiles (LKPs) in a cohort of zebrafish embryos

(A and B) Comparison of the LKPs' mean (line) and variance (shaded area), calculated for selected cell populations (selection at the tail bud stage, Figure S8, Video S22), hypoblast (red) and epiblast (blue) in embryos *wt1-wt5* (rows 1 through 5, respectively).

(A) Instantaneous LKPs. Time in hpf. The vertical dashed black line indicates the onset of epiblast compression chosen as the initial time (t_{ini}).

(B) LKPs cumulated from (t_{ini}) for the next 6 h, mean (line) and variance (shaded area). The five plots are aligned in time using t_{ini} as reference. Hypoblast was not analyzed in embryo *wt2* as it was not detected at t_{ini} because of that embryo's position in the field of view.

Lagrangian ΔV and Eulerian P are compared since both descriptors quantify compression/expansion). These data are represented during the interval 9–12 hpf, corresponding to mid-late gastrulation. Overall, the Lagrangian descriptors exhibited patterns that were more coherent in space and persistent in time than the Eulerian descriptors (Figure 3; Figure S7). These Lagrangian metrics revealed territories at the whole embryo scale that experienced distinct, reproducible cumulative deformations while their instantaneous deformations had a comparatively large variability. These cumulative deformations should provide useful quantitative information about the mechanical stimuli experienced by cells during development.

Inter-specimen variability of tissue deformation patterns

To investigate the similarity of instantaneous and cumulative tissue deformation between wild-type zebrafish embryos, we calculated the mean Eulerian and Lagrangian deformation metrics for manually segmented epiblast and hypoblast cell populations in five specimens[42] (tail bud selection, Figure S8; Videos S21 and S22). The time progression of Eulerian mean deformations in both tissues (Figure 4A) shows inter-specimen variability and temporal fluctuations along gastrulation. The onset of epiblast compression corresponding with $P = 0$ (dashed lines between 7 and 8 hpf in Figure 4A) was taken as a landmark to temporally align the different datasets and as a reference state to calculate the Lagrangian cumulative deformation metrics (Figure 4B). Consistent with Figure 3, the temporal profiles of cumulative tissue deformations of the hypoblast and epiblast behaved smoothly. More importantly, the epiblast and hypoblast showed distinct profiles of mean cumulative deformations that were similar in all specimens.

Unsupervised classification of cumulative tissue deformation in wild-type and mutant embryos

Given our data suggesting that the hypoblast and epiblast experienced distinct, reproducible cumulative deformation

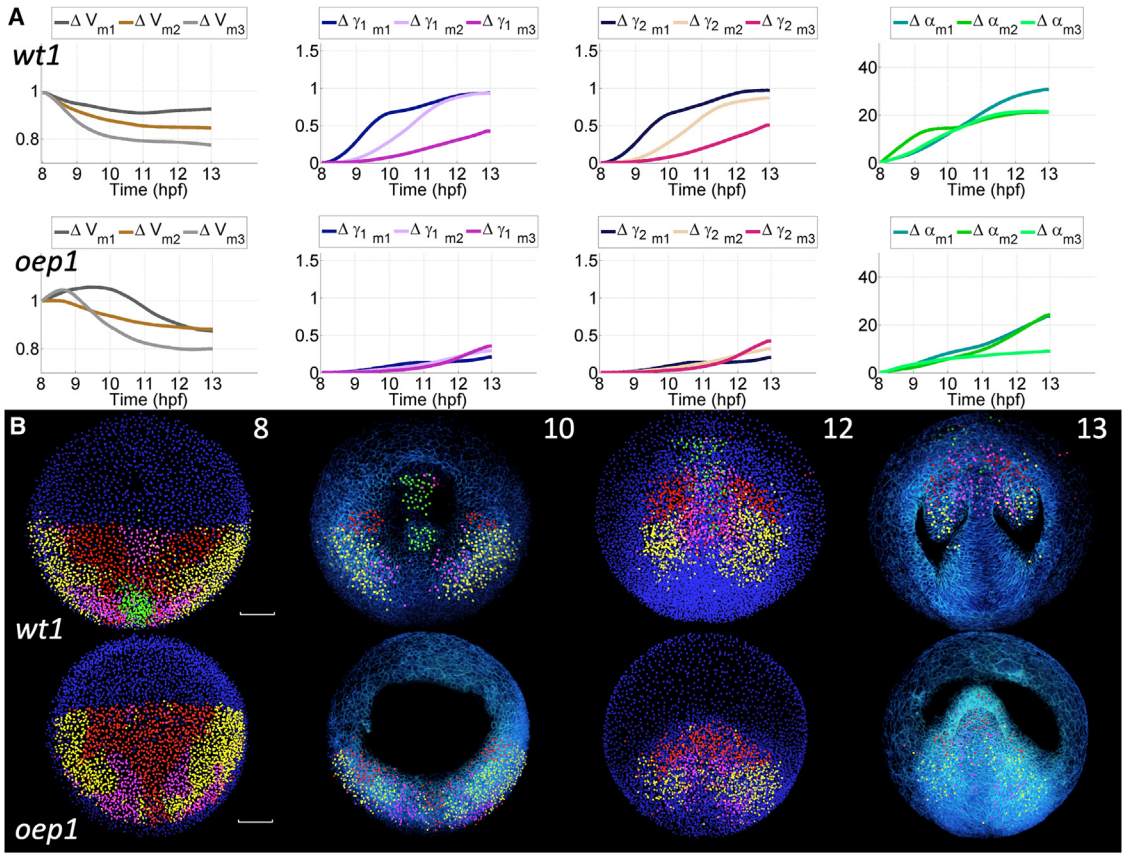

Figure 5. Unsupervised clustering and reduced-order models of cumulative deformation in normal and *oep* mutant embryos: Canonical Lagrangian Kinematic Profiles and Biomechanical Maps

(A) Mean (subindex m) time course of cumulative deformation metrics (e.g., ΔV) for each of the three clusters (number of clusters identified as optimal, see Figures S10 and S12) define the canonical Lagrangian kinematic profiles (CLKPs) in the wild type embryo (top row) and the mutant (bottom row). Lines are color-coded to differentiate the three CLKPs. For ΔV, values higher and lower than 1 indicate expansion and compression, respectively. For $\Delta\gamma_1$ and $\Delta\gamma_2$, the values range from no distortion (0) to maximum distortion (3). For $\Delta\alpha$, the value represents rotation angles in degrees.

(B) Reduced-order biomechanical maps obtained for *wt1* and *oep1* embryos. Cells at t_{ini} = 8 hpf were selected in Mov-IT and clustered according to their Lagrangian biomechanical signature (9-component vector expressing the similarity of each trajectory's Lagrangian deformation metrics to the CLKPs, see Figure S13). Four and three distinct domains (clusters) were obtained for the *wt1* and *ope1* embryos, respectively, and color-labeled at t_{ini} = 8 hpf. This color code was propagated along the cell lineages belonging to each domain (time point indicated at the top right corner of the top row panels, expressed in hpf). At 8 and 12 hpf, unlabeled nuclei in blue. At 10 and 13 hpf, the labeled nuclear centers are displayed together with the membrane raw data (3D rendering in blue). The upper sections were removed down to 65 μm below the embryo surface to facilitate visualization. Scale bar 50 μm. First row: *wt1* embryo (Videos S23, S24, and S25). Second row: *oep1* embryo (Video S26).

profiles, we investigated whether unsupervised classification of these profiles would identify spatially homogeneous regions. Thus, we applied k-means clustering to the temporal profiles of Lagrangian deformation metrics along each cell trajectory enclosed in the field of view from 8 to 14 hpf (shield-stage selection, Figure S9). The selected cell population is located at the animal pole of the early gastrula and is expected to encompass the presumptive forebrain and the prechordal plate.[29] Similarities amongst deformation profiles were estimated using a cosine distance that balanced the differences in range and temporal evolution. Figure 5A displays three clusters' k-mean profiles for each Lagrangian deformation descriptor. These clusters represent different levels, rates, and phases of cumulative compression (ΔV), angular distortion ($\Delta\gamma_1$ and $\Delta\gamma_2$), and rotation ($\Delta\alpha$). Three clusters sufficed to characterize the diversity of cumulative deformation profiles within the selected cell population, as the k-mean profiles obtained by increasing the number of clusters did not add significant information (Figure S10). These three clusters were reproducible across different specimens (Figure S11). Of note, the hypoblast's cumulative deformation descriptors were captured by one single k-mean profile (Figure S12A), while the other two k-mean profiles corresponded to the epiblast (Figure S12B). These results suggest that unsupervised machine learning can condense the complex spectrum of tissue deformations experienced by cells during early development into a reduced number of distinct, reproducible, and interpretable temporal profiles of cumulative deformation. Hereafter, we denote these profiles as canonical Lagrangian kinematic profiles (CLKPs).

Morphogenetic defects such as those leading to cyclopia caused major biomechanical perturbations at an early developmental stage. CLKPs in *zoep*$^{tz57/tz57}$ mutants differed from wild-type. In *zoep*$^{tz57/tz57}$ mutants, unsupervised clustering produced three CLKPs (Figure 5A) that had an initial phase of expansion instead of sustained compression, reduced angular distortion, and reduced rotation compared to wild-type.

Reduced-order models of tissue deformation in wild-type and *zoep*$^{tz57/tz57}$ mutant embryos

We leveraged the CLKPs to develop reduced-order models of tissue deformation and tested whether these models map spatiotemporally coherent domains in the developing embryo. Every cell trajectory was labeled with a 9-element vector of zeros and ones categorizing the similarity between the Lagrangian deformation descriptors (ΔV, $\Delta\gamma_1$, $\Delta\alpha$) and the three CLKPs associated with each descriptor. For instance, a cell trajectory whose ΔV was closest to the third ΔV-CLKP, the third $\Delta\gamma_1$-CLKP, and the second $\Delta\alpha-$CLKP would be labeled by ζ = (0,0,1,0,0,1,0,1,0) (Figure S13). We denoted this vector ζ as the cell's biomechanical "signature". We then performed hierarchical clustering to identify four groups of cells with similar biomechanical signatures and tracked the clusters' spatial organization during development (Figures 5B and S14; Videos S23 and S24). We then performed hierarchical clustering to identify four groups of cells with similar biomechanical signatures and tracked the clusters' spatial organization during development (Figures 5B and S14; Videos S23 and S24). The resulting cell populations formed spatially connected, bilaterally symmetrical domains that remained coherent throughout the imaging period. These biomechanical domains can be compared with the state-of-the-art brain fate map[29–31] to establish correlations between the history of mechanical cues experienced by cells and their fate.

We used the interactive visualization software Mov-IT to compare the biomechanical domains identified by unsupervised machine learning (Figure 5B) and the morphological compartments identified by fluorescent staining of the cell membrane. The fields of the prechordal plate and the ventral forebrain at the midline (presumptive hypothalamus) were included in the green domain (Figure 5B), indicating that these two fields experienced similar sequences of mechanical events, which in turn highlights the role of the prechordal plate in the formation of the brain and the separation of the eye field to form bilateral eyes. In particular, they underwent an early increase in distortion and rotation followed by a rigid anterior displacement over the yolk. The three other biomechanical domains (marked with yellow, pink, and red in Figure 5B) matched the eye field and, likely, part of the ventral brain. The eye field appeared to contain three domains with different mechanical histories: (1) a most ventral domain (yellow) that underwent the steepest temporal increase in rotation by the end of gastrulation, (2) a ventral medial domain (pink) that underwent late distortion and low-to-intermediate compression, and (3) a ventral lateral domain (red) subjected to the highest increase in compression during gastrulation and early neurulation (Figures S15–S17, Videos S23, S24, and S25).

A similar approach was applied to the zo*ep*$^{tz57/tz57}$ mutants, which are defective in the transduction of Nodal signals and lack endoderm and the endomesodermal cells that constitute the prechordal plate[43] (Video S26). In these mutants, hierarchical clustering of cell trajectories based on their CLKPs produced three biomechanical domains instead of the four domains found in wild-type embryos (Figure 5B). The missing domain in *zoep*$^{tz57/tz57}$ embryos was the midline green domain characterized by high shear activity. The conserved domains in *zoep*$^{tz57/tz57}$ embryos were distributed spatially as in wild-type embryos at the initial time point of the analysis (8 hpf). However, their convergence toward the midline, subsequent antero-posterior extension along the body axis, and eventual bilateral rotation were significantly delayed. These data suggest that the midline acts as an attractor-repeller structure in wild-type embryos while it only retains its attractor activity in *zoep*$^{tz57/tz57}$ mutants. This abnormality leads to the absence of counter-rotating vortices (Videos S9 and S10) and to the absence of separation of the red biomechanical domain at the midline (Figure 5B, red domain), which are consistent with a unique eye field that leads to cyclopia. Altogether, we propose that unsupervised machine learning can produce morphological maps with a few domains that follow distinct sequences of mechanical cues. These maps contribute to better understand large-scale collective cell movements involved in the organization of morphogenetic fields and how these processes are affected by genetic and environmental perturbations.

Correlation between reduced-order models of tissue deformation and gene expression

We hypothesized that the "green" biomechanical domain matched the prechordal plate. To test this hypothesis, and to demonstrate that biomechanical domains are associated with cell fate, we imaged *Tg(gsc:EGFP)* transgenic embryos with fluorescently labeled prechordal plate.[44] Images were processed to construct a reduced-order model for the spatiotemporal dynamics of the *goosecoid* gene reporter expression (Figure 6, Video S27). Three canonical gene expression profiles were identified according to the range and temporal dynamics of fluorescence (green, medium in cyan, and low in blue, Figures 6A and S18). The level of expression of the fluorescent reporter along cell trajectories was calibrated (STAR Methods, Figures 6B and 6C). Based on these canonical profiles, we built a reduced-order model with three time-evolving genetic domains (Figure 6D). Then, we performed the unsupervised analysis of Lagrangian deformation descriptors as in the previous sections to obtain a reduced-order biomechanical model in the same embryo. This analysis yielded four biomechanical domains (Figures 6E; Video S27) that behaved as expected for a wild-type embryo (Figures 5B and S14, Video S23). Comparing the genetic and biomechanical domains in the transgenic embryos revealed that the high *gsc* reporter expression domain (Figure 6D, green) overlaps with the high shear biomechanical domain (Figure 6E, green), meaning that *gsc* expression in the prechordal plate is associated with a distinct morpho-mechanical activity.

Conclusion

The 4D kinematic analysis of digitally reconstructed cell lineage trees, based on 3D + time imaging of developing

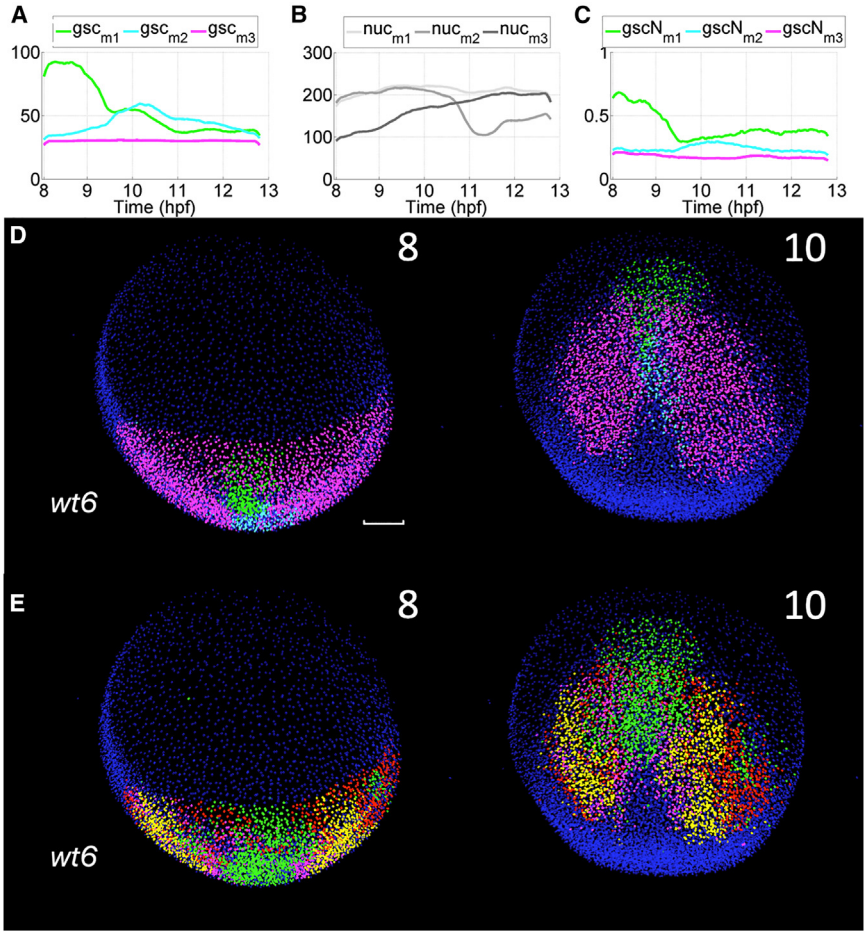

Figure 6. Reduced-order models of tissue deformation and *gsc* reporter expression yield corresponding maps (A – E) *wt6* embryo from the transgenic line *Tg(gsc:EGFP)* (STAR Methods) imaged from 8 to 13 hpf

(A) Quantification of *gsc* reporter expression at the single cell level (STAR Methods, Table S1) and k-means clustering of cell populations according to the reporter expression level (k = 3 green -gsc_{m1}-, light blue -gsc_{m2}- and magenta -gsc_{m3}- for the mean expression level in each cluster).

(B) Average time course of nuclear staining intensity along cell trajectories for each cluster: nuc_{m1}, nuc_{m2} and nuc_{m3}.

(C) Average value of the *gsc* reporter expression along each cluster's cell trajectories, normalized by nuclear staining intensity ($gscN_{m1}$, $gscN_{m2}$ and $gscN_{m3}$).

(D) Reduced-order maps of *gsc* reporter expression showing three domains and their spatiotemporal organization (green -gsc_{m1}-, light blue -gsc_{m2}- and magenta -gsc_{m3}, time points 8 and 10 hpf indicated top right of each panel). Cells at 8 hpf are color-labeled according to the cluster they belong to and the color is propagated along the cell lineage.

(E) Reduced-order biomechanical map showing four domains and their spatiotemporal organization similar to *wt1* in Figure 5 (time points 8 and 10 hpf indicated top right of each panel, t_{ini} = 8 hpf). Scale bar 50 μm.

organisms, is an advanced approach to study cell and tissue dynamics in morphogenesis.[45] The quantitative features of our datasets enable the construction of mechanistic models. However, the extraction of meaningful information from this massive amount of data challenges existing methods. State-of-the-art computational workflows have been designed to process time-lapse imaging datasets and achieve cell tracking in space and time. However, these approaches have their limitations and do not produce error-free lineage trees,[35,36] especially in the case of vertebrate organisms with high cell density and thick tissues. The typical 2% of false links per time step requires manual corrections to retrieve cells' complete history. We show that this somewhat noisy data can be used for kinematics by conceptualizing tissue deformation as a flow,[46] which is valid for tissues that display either fluid-like[47] or solid-like[48–50] behavior.

We computed tissue deformation descriptors from digital cell lineages and applied machine learning to build the biomechanical signature of every cell along its trajectory. The Eulerian description, based on incremental deformation metrics expressed on a coordinate system fixed in the imaging field of view, marks the transitions that happen during zebrafish gastrulation and provides a functional developmental table. Eulerian deformation metrics give rise to coherent patterns at the scale of morphogenetic fields. Besides, the Lagrangian description, based on finite deformation metrics measured over segments of each cell's trajectory, are less sensitive to noise and inter-specimen variability. Lagrangian metrics robustly capture the 4D spatiotemporal tissue motions that shape the embryo. Embryonic tissues undergo distinct time courses of cumulative deformation (CLKPs) that can be identified reproducibly by unsupervised machine learning. For the investigated temporal window encompassing gastrulation, we found that a few (i.e., ~3) CLKPs are sufficient to characterize the diversity of temporal deformation experienced by the embryonic tissues.

We showed that CLKPs can be used as a basis to build reduced-order models of tissue deformation that demarcate the boundaries between embryonic domains with distinct 4D biomechanics. Furthermore, these "biomechanical domains" match spatiotemporal gene expression patterns. Specifically, we applied our unsupervised analysis to wild-type embryos and nodal pathway mutants ($zoep^{tz57/tz57}$) that develop cyclopia to illustrate how the prechordal plate migration goes with tissue deformation that impacts the bilateral symmetry, eye and forebrain formation. We identified that the prechordal plate, marked by the expression of the transcription factor *goosecoid* has a specific biomechanical signature. While these data are not sufficient to infer causality between biomechanical cues, gene expression and cell fate, our analysis pipeline can be applied to large 3D + time image datasets from different species to demonstrate their correlation.

Table 1. List of imaged embryos and imaging conditions

Embryo	ID	Voxel	Voxel Size (μm^3)	Timestep	Duration (hpf)	T° (°C)	T° control
wt1	071226a	512 × 512 × 120	1.37	2′33″	5.5–15	26	21° room
wt2	140523aF	512 × 512 × 177	1.26	2′28″	5–13.8	26	Okolab
wt3	141106aF	512 × 512 × 148	1.38	2′24″	6–18	26	Okolab
wt4	141108aF	512 × 512 × 174	1.38	2′26″	6.5–20	28.6	Okolab
wt5	141108a	512 × 512 × 172	1.37	2′25″	6.5–20	24.7	Okolab
wt6	091021aF	512 × 512 × 238	1.51	3′01″	2.75–22.5	26	22° room
oep1	081018a	512 × 512 × 171	1.31	2′31″	4–22.2	26	22° room
oep2	081025a	512 × 512 × 179	1.31	2′38″	3.25–21.1	26	22° room
oep3	120914aF	512 × 512 × 114	1.51	2′31″	5.9-22-9	26	22° room
oep4	170315aF	512 × 512 × 167	1.51	1′40″	6–16.5	26	Okolab
oep5	170321aF	512 × 512 × 177	1.38	2′13″	5–18.3	26	Okolab

Together with a constitutive equation capturing the relationship between spatially and temporally heterogeneous stresses/strains within embryonic tissues, the approach introduced in this study could help uncover the role of mechanical forces in morphogenesis. In recent years, the measurement of embryonic tissue properties and mechanical forces has experienced significant advances.[51,52] However, the comprehensive quantification of stress and strain along all the cell trajectories in the whole organism remains challenging. Although the forces driving zebrafish gastrulation remain to be fully determined, our study shows that displacement of the hypoblast relative to the epiblast at the dorsal midline generates bilateral jet-vortices that shape the anterior brain and ensures the formation of bilateral eyes.

In summary, we show that 4D measurements of tissue deformation along cells' trajectory throughout gastrulation can be exploited by unsupervised machine learning to delineate morphological domains subjected to distinct biomechanical cues. We show that these biomechanical domains correlate with gene expression patterns. We introduce a conceptual and analysis framework, well suited for large-scale collective cell displacements, to identify, classify, and interpret 4D patterns of collective cell movement during development and their relationship with cell fate.

Limitations of the study

Our methodology is based on velocity fields derived from cell trajectories and the measurement of tissue deformation. The available data gives access to strain but does not document the forces that generate the strains.

The number of imaged specimens (five wild-type, five *oep* mutants, and one wild-type with *gsc* reporter expression) allowed us to design and validate the methodology. A larger number of specimens would be necessary to extract statistically powered biological results, quantitatively assess the variability for the zebrafish strain and construct prototypic specimens.

The spatiotemporal regularization of the cell velocity field, necessary to ensure differentiability for computing strains and strain rates smooths out the gradients and likely causes to underestimate the metrics. As described above, we tested several filter widths to find an optimal value (R = 20 μm) that minimally dampened the displacement gradients (Figure S2). Finally, it should be noted that the machine learning classification performed in this study was relatively unsophisticated. Rather than being a limitation, it implies that the biomechanical domains are robust and do not depend on the chosen classification models.

RESOURCE AVAILABILITY

Lead contact

Further information and requests for resources and reagents should be directed to and will be fulfilled by the lead contact David Pastor-Escuredo (david@lifedlab.org).

Materials availability

- Embryo 4D datasets were generated for this study with a total of six wild-type embryos and five mutant embryos. Datasets can be downloaded from the BioEmergences database upon request and have been deposited in Mendeley. DOIs are listed in the key resources table.
- Digital lineages were generated for this study with a total of six wild-type embryos and five mutant embryos. Lineages can be downloaded through the BioEmergences software tool Mov-It and have been deposited in Mendeley. DOIs are listed in the key resources table.
- Kinematic descriptors and Biomechanical maps were generated for this study. They can be readily computed using the code over the cell lineage.

Data and code availability

- Movies, raw images, and cell lineage data are available on the BioEmergences website: http://bioemergences.eu/kinematics/login: kinematics password: AGBYeL4y
- Raw data and cell lineage data has been deposited at Mendeley Data with one DOI per dataset including raw imaging data and cell tracking as Mendeley Data: https://doi.org/10.17632/vnpczd3hjk.1 and so on and are publicly available as of the date of publication. The DOI of each dataset is listed in the key resources table. The datasets can be searched and found as this "BioEmergences-wt1" at Mendeley Data, etc.
- All original code has been deposited at Github https://github.com/dpastoresc/EmbryoKinematicsFramework and is publicly available at https://doi.org/10.5281/zenodo.14698253 as of the date of publication. DOIs are listed in the key resources table. The release of the code has been made under version v1.0.0 "EmbryoKinematicsFramework iScience January 2025" at the corresponding Github repository.

ACKNOWLEDGMENTS

We thank the BioEmergences laboratory, especially Louise Duloquin and Dimitri Fabrèges for their collaboration and support. This work was supported in part by Ministerio de Ciencia e Innovación, Agencia Estatal de Investigación (Spain), under grants PDC2022-133865-I00 and PID2022-141493OB-I00, co-financed by European Regional Development Fund (ERDF), 'A way of making Europe', by MAGERIT-CM grant (TEC-2024/COM-44) funded by Comunidad de Madrid for M.J.L.C and ASL, by grants Project# 1R01HD092216-01A1, NSF CBET – 1055697, NIH R01 GM084227, NIH 1R01HL170607-01A1, NIH NIAID R01AI167943, NIH R01HD106628 for J.-C.A. and by grants EU NEST-2004-Path-IMP - 28892, ZF-Health EU project HEALTH-F4-2010-242048, ANR BioSys Morphoscale, France BioImaging infrastructure ANR-10-INBS-04, ANR-11-EQPX-029 and InterDIM 2011 Région Paris Ile-de-France to N.P. and P.B. D.P-E. would like to acknowledge the Social Council of Universidad Politécnica de Madrid for supporting this work through a special scholarship.

AUTHOR CONTRIBUTIONS

D.P. developed the framework, designed visualization and analysis, interpreted the results, and co-wrote the manuscript. B.L. designed and developed the foundation of the study. T.S. developed the visualization and co-wrote the manuscript. A.B. carried out biological experimentation and imaging. R.D. supervised the final version of the Methods and edited the manuscript. J.G. supervised the physics foundations of the methods. A.S. co-funded and co-coordinated the project. P.B. co-funded and co-coordinated the project and supervised the foundation of the study. J.C.A. co-funded and co-coordinated the project, supervised the physics foundation of the project. and co-wrote the manuscript. M.J.L. co-funded and co-coordinated the project, supervised the design of the analysis framework, and co-wrote the manuscript. N.P. co-funded and co-coordinated the project, supervised data acquisition and analysis, led the biological interpretation, and co-wrote the manuscript.

DECLARATION OF INTERESTS

The authors declare no competing financial interests.

STAR★METHODS

Detailed methods are provided in the online version of this paper and include the following:

- KEY RESOURCES TABLE
- EXPERIMENTAL MODEL AND SUBJECT DETAILS
- METHOD DETAILS
  - In-vivo imaging
  - Flow field approximation of cell lineage
  - Instantaneous deformation descriptors
  - Building Lagrangian Kinematic Profiles
  - Computation of FTDG tensors and descriptors
  - Visualization of descriptor maps and manual selection of cell domains
  - Categorization of Lagrangian Kinematic Profiles
- QUANTIFICATION AND STATISTICAL ANALYSIS
  - Reduced-order models of Lagrangian tissue deformation: Biomechanical domains
  - Reduced-order models of *gsc* expression: morphogenetic domains
  - Lagrangian comparison of embryo specimens based on their LKPs
- ADDITIONAL RESOURCES

SUPPLEMENTAL INFORMATION

Supplemental information can be found online at https://doi.org/10.1016/j.isci.2025.111753.

Received: September 28, 2021
Revised: April 30, 2022
Accepted: January 3, 2025
Published: January 9, 2025

REFERENCES

1. Heisenberg, C.P., and Bellaïche, Y. (2013). Forces in Tissue Morphogenesis and Patterning. Cell *153*, 948–962.
2. Lecuit, T., Lenne, P.F., and Munro, E. (2011). Force generation, transmission, and integration during cell and tissue morphogenesis. Annu. Rev. Cell Dev. Biol. *27*, 157–184.
3. Bosveld, F., Bonnet, I., Guirao, B., Tlili, S., Wang, Z., Petitalot, A., Marchand, R., Bardet, P.L., Marcq, P., Graner, F., and Bellaïche, Y. (2012). Mechanical control of morphogenesis by Fat/Dachsous/Four-jointed planar cell polarity pathway. Science *336*, 724–727.
4. Bosveld, F., Markova, O., Guirao, B., Martin, C., Wang, Z., Pierre, A., Balakireva, M., Gaugue, I., Ainslie, A., Christophorou, N., et al. (2016). Epithelial tricellular junctions act as interphase cell shape sensors to orient mitosis. Nature *530*, 495–498.
5. Blanchard, G.B., and Adams, R.J. (2011). Measuring the multi-scale integration of mechanical forces during morphogenesis. Curr. Opin. Genet. Dev. *21*, 653–663.
6. Davidson, L., von Dassow, M., and Zhou, J. (2009). Multi-scale mechanics from molecules to morphogenesis. Int. J. Biochem. Cell Biol. *41*, 2147–2162.
7. Keller, R. (2012). Physical biology returns to morphogenesis. Science *338*, 201–203.
8. Gilmour, D., Rembold, M., and Leptin, M. (2017). From morphogen to morphogenesis and back. Nature *541*, 311–320.
9. Olivier, N., Luengo-Oroz, M.A., Duloquin, L., Faure, E., Savy, T., Veilleux, I., Solinas, X., Débarre, D., Bourgine, P., Santos, A., et al. (2010). Cell Lineage Reconstruction of Early Zebrafish Embryos Using Label-Free Nonlinear Microscopy. Science *329*, 967–971.
10. Supatto, W., Truong, T.V., Débarre, D., and Beaurepaire, E. (2011). Advances in multiphoton microscopy for imaging embryos. Curr. Opin. Genet. Dev. *21*, 538–548.
11. Keller, P.J. (2013). Imaging Morphogenesis: Technological Advances and Biological Insights. Science *340*, 1234168.
12. Gao, L., Shao, L., Chen, B.C., and Betzig, E. (2014). 3D live fluorescence imaging of cellular dynamics using Bessel beam plane illumination microscopy. Nat. Protoc. *9*, 1083–1101.
13. Steigmaier, J., Amat, F., Lemon, W.C., McDole, K., Wan, Y., Teodoro, G., Mikut, R., and Keller, P.J. (2016). Real-Time Three-Dimensional Cell Segmentation in Large-Scale Microscopy Data of Developing Embryos. Dev. Cell *36*, 225–240.
14. Wolff, C., Tinevez, J.Y., Pietzsch, T., Stamataki, E., Harich, B., Guignard, L., Preibisch, S., Shorte, S., Keller, P.J., Tomancak, P., et al. (2018). Multi-view light-sheet imaging and tracking with the MaMuT software reveals the cell lineage of a direct developing arthropod limb. Elife *7*, e34410.
15. Liu, T.L., Upadhyayula, S., Milkie, D.E., Singh, V., Wang, K., Swinburne, I.A., Mosaliganti, K.R., Collins, Z.M., Hiscock, T.W., Shea, J., et al. (2018). Observing the cell in its native state: Imaging subcellular dynamics in multicellular organisms. Science *360*, eaaq1392.
16. Ovečka, M., von Wangenheim, D., Tomančák, P., Šamajová, O., Komis, G., and Šamaj, J. (2018). Multiscale imaging of plant development by light-sheet fluorescence microscopy. Nat. Plants *4*, 639–650.
17. McMahon, A., Supatto, W., Fraser, S.E., and Stathopoulos, A. (2008). Dynamic analyses of Drosophila gastrulation provides insights into collective cell migration. Science *322*, 1546–1550.
18. Behrndt, M., Salbreux, G., Campinho, P., Hauschild, R., Oswald, F., Roensch, J., Grill, S.W., and Heisenberg, C.P. (2012). Forces Driving

Epithelial Spreading in Zebrafish Gastrulation. Science *338*, 257–260.

19. Blanchard, G.B., Kabla, A.J., Schultz, N.L., Butler, L.C., Sanson, B., Gorfinkiel, N., Mahadevan, L., and Adams, R.J. (2009). Tissue tectonics: morphogenetic strain rates, cell shape change and intercalation. Nat. Methods *6*, 458–464.
20. Tetley, R.J., Blanchard, G.B., Fletcher, A.G., Adams, R.J., and Sanson, B. (2016). Unipolar distributions of junctional Myosin II identify cell stripe boundaries that drive cell intercalation throughout Drosophila axis extension. Elife *5*, e12094.
21. Graner, F., Dollet, B., Raufaste, C., and Marmottant, P. (2008). Discrete rearranging disordered patterns, part I: Robust statistical tools in two or three dimensions. Eur. Phys. J. E Soft Matter *25*, 349–369.
22. Brodland, G.W., Conte, V., Cranston, P.G., Veldhuis, J., Narasimhan, S., Hutson, M.S., Jacinto, A., Ulrich, F., Baum, B., and Miodownik, M. (2010). Video force microscopy reveals the mechanics of ventral furrow invagination in Drosophila. Proc. Natl. Acad. Sci. USA *107*, 22111–22116.
23. Chiou, K.K., Hufnagel, L., and Shraiman, B.I. (2012). Mechanical Stress Inference for Two Dimensional Cell Arrays. PLoS Comput. Biol. *8*, e1002512.
24. Ishihara, S., and Sugimura, K. (2012). Bayesian inference of force dynamics during morphogenesis. J. Theor. Biol. *313*, 201–211.
25. Tlili, S., Gay, C., Graner, F., Marcq, P., Molino, F., and Saramito, P. (2015). Colloquium: Mechanical formalisms for tissue dynamics. Eur. Phys. J. E Soft Matter *38*, 121–131.
26. Veldhuis, J.H., Ehsandar, A., Maître, J.L., Hiiragi, T., Cox, S., and Brodland, G.W. (2017). Inferring cellular forces from image stacks. Phil. Trans. R. Soc. B. *372*, 20160261.
27. Woo, K., and Fraser, S.E. (1995). Order and coherence in the fate map of the zebrafish nervous system. Development *121*, 2595–2609.
28. Loganathan, R., Little, C.D., Joshi, P., Filla, M.B., Cheuvront, T.J., Lansford, R., and Rongish, B.J. (2014). Identification of emergent motion compartments in the amniote embryo. Organogenesis *10*, 350–364.
29. Chan, C.J., Heisenberg, C.-P., and Hiiragi, T. (2017). Coordination of morphogenesis and cell-fate specification in development. Curr. Biol. *27*, R1024–R1035.
30. Polacheck, W.J., and Chen, C.S. (2016). Measuring cell-generated forces: a guide to the available tools. Nat. Methods *13*, 415–423.
31. Roca-Cusachs, P., Conte, V., and Trepat, X. (2017). Quantifying forces in cell biology. Nat. Cell Biol. *19*, 742–751.
32. Keller, R. (2002). Shaping the vertebrate body plan by polarized embryonic cell movements. Science *298*, 1950–1954.
33. Solnica-Krezel, L., and Sepich, D.S. (2012). Gastrulation: making and shaping germ layers. Annu. Rev. Cell Dev. Biol. *28*, 687–717.
34. Mitrossilis, D., Röper, J.C., Le Roy, D., Driquez, B., Michel, A., Ménager, C., Shaw, G., Le Denmat, S., Ranno, L., Dumas-Bouchiat, F., et al. (2017). Mechanotransductive cascade of Myo-II-dependent mesoderm and endoderm invaginations in embryo gastrulation. Nat. Commun. *8*, 13883.
35. Amat, F., Lemon, W., Mossing, D.P., McDole, K., Wan, Y., Branson, K., Myers, E.W., and Keller, P.J. (2014). Fast, accurate reconstruction of cell lineages from large-scale fluorescence microscopy data. Nat. Methods *11*, 951–958.
36. Faure, E., Savy, T., Rizzi, B., Melani, C., Stašová, O., Fabrèges, D., Špir, R., Hammons, M., Čúnderlík, R., Recher, G., et al. (2016). A workflow to process 3D+time microscopy images of developing organisms and reconstruct their cell lineage. Nat. Commun. *7*, 8674.
37. Wagner, D.E., Weinreb, C., Collins, Z.M., Briggs, J.A., Megason, S.G., and Klein, A.M. (2018). Single-cell mapping of gene expression landscapes and lineage in the zebrafish embryo. Science *360*, 981–987.
38. Briggs, J.A., Weinreb, C., Wagner, D.E., Megason, S., Peshkin, L., Kirschner, M.W., and Klein, A.M. (2018). The dynamics of gene expression in vertebrate embryogenesis at single-cell resolution. Science *360*, eaar5780.
39. Zhang, J., Talbot, W.S., and Schier, A.F. (1998). Positional cloning identifies zebrafish one-eyed pinhead as a permissive EGF-related ligand required during gastrulation. Cell *92*, 241–251.
40. Holzapfel, G.A. (2002). Nonlinear solid mechanics: a continuum approach for engineering science. Meccanica *37*, 489–490.
41. Chong, M.S., Perry, A.E., and Cantwell, B.J. (1990). A general classification of three-dimensional flow fields. Phys. Fluid. Fluid Dynam. *2*, 765–777.
42. Kimmel, C.B., Ballard, W.W., Kimmel, S.R., Ullmann, B., and Schilling, T.F. (1995). Stages of embryonic development of the zebrafish. Dev. Dynam. *203*, 253–310.
43. England, S.J., Blanchard, G.B., Mahadevan, L., and Adams, R.J. (2006). A dynamic fate map of the forebrain shows how vertebrate eyes form and explains two causes of cyclopia. Development *133*, 4613–4617.
44. Joore, J., Fasciana, C., Speksnijder, J.E., Kruijer, W., Destrée, O.H., van den Eijnden-van Raaij, A.J., de Laat, S.W., Zivkovic, D., and Zivkovic, D. (1996). Regulation of the zebrafish goosecoid promoter by mesoderm inducing factors and Xwnt1. Mech. Dev. *55*, 3–18.
45. Delile, J., Herrmann, M., Peyriéras, N., and Doursat, R. (2016). MecaGen: a cell-based computational model of embryogenesis coupling mechanical behavior and gene regulation. Nat. Commun. *7*. In press.
46. He, B., Doubrovinski, K., Polyakov, O., and Wieschaus, E. (2014). Apical constriction drives tissue-scale hydrodynamic flow to mediate cell elongation. Nature *508*, 392–396.
47. Fleury, V., Chevalier, N.R., Furfaro, F., and Duband, J.L. (2015). Buckling along boundaries of elastic contrast as a mechanism for early vertebrate morphogenesis. Eur. Phys. J. E Soft Matter *38*, 9.
48. Mongera, A., Rowghanian, P., Gustafson, H.J., Shelton, E., Kealhofer, D.A., Carn, E.K., Serwane, F., Lucio, A.A., Giammona, J., and Campàs, O. (2018). A fluid-to-solid jamming transition underlies vertebrate body axis elongation. Nature *561*, 401–405.
49. Petridou, N.I., Grigolon, S., Salbreux, G., Hannezo, E., and Heisenberg, C.P. (2019). Fluidization-mediated tissue spreading by mitotic cell rounding and non-canonical Wnt signalling. Nat. Cell Biol. *21*, 169–178.
50. Petridou, N.I., Corominas-Murtra, B., Heisenberg, C.P., and Hannezo, E. (2021). Rigidity percolation uncovers a structural basis for embryonic tissue phase transitions. Cell *184*, 1914–1928.
51. Campàs, O., Mammoto, T., Hasso, S., Sperling, R.A., O'Connell, D., Bischof, A.G., Maas, R., Weitz, D.A., Mahadevan, L., and Ingber, D.E. (2014). Quantifying cell-generated mechanical forces within living embryonic tissues. Nat. Methods *11*, 183–189.
52. Serwane, F., Mongera, A., Rowghanian, P., Kealhofer, D.A., Lucio, A.A., Hockenbery, Z.M., and Campàs, O. (2017). In vivo quantification of spatially varying mechanical properties in developing tissues. Nat. Methods *14*, 181–186.
53. Moriyoshi, K., Richards, L.J., Akazawa, C., O'Leary, D.D., and Nakanishi, S. (1996). Labeling neural cells using adenoviral gene transfer of membrane-targeted GFP. Neuron *16*, 255–260.
54. Shaner, N.C., Steinbach, P.A., and Tsien, R.Y. (2005). A guide to choosing fluorescent proteins. Nat. Methods *2*, 905–909.
55. Westerfield, M. (2000). The Zebrafish Book: A Guide for the Laboratory Use of Zebrafish (Danio rerio) (University of Oregon Press).
56. So, P.T., Dong, C.Y., Masters, B.R., and Berland, K.M. (2000). Two-photon excitation fluorescence microscopy. Annu. Rev. Biomed. Eng. *2*, 399–429.
57. CRAMiR, H., and Leadbetter, M.R. (1967). Stationary and Related Stochastic Processes (New York: JohnWiley).

58. Shadden, S.C., Lekien, F., and Marsden, J.E. (2005). Definition and properties of Lagrangian coherent structures from finite-time Lyapunov exponents in two-dimensional aperiodic flows. Phys. Nonlinear Phenom. *212*, 271–304.

59. Haller, G. (2015). Lagrangian coherent structures. Annu. Rev. Fluid Mech. *47*, 137–162.

60. Castro-González, C., Luengo-Oroz, M.A., Duloquin, L., Savy, T., Rizzi, B., Desnoulez, S., Doursat, R., Kergosien, Y.L., Ledesma-Carbayo, M.J., Bourgine, P., et al. (2014). A digital framework to build, visualize and analyze a gene expression atlas with cellular resolution in zebrafish early embryogenesis. PLoS Comput. Biol. *10*, e1003670.

STAR★METHODS

KEY RESOURCES TABLE

REAGENT or RESOURCE	SOURCE	IDENTIFIER
Deposited data		
Digital embryo zebrafish wild-type wt1	CNRS-BioEmergences, this paper, Mendeley Data	Mendeley Data: https://doi.org/10.17632/vnpczd3hjk.1
Digital embryo zebrafish wild-type wt2	CNRS-BioEmergences, this paper, Mendeley Data	Mendeley Data: https://doi.org/10.17632/dtt28wk335.1
Digital embryo zebrafish wild-type wt3	CNRS-BioEmergences, this paper, Mendeley Data	Mendeley Data: https://doi.org/10.17632/vcgbmpr366.1
Digital embryo zebrafish wild-type wt4	CNRS-BioEmergences, this paper, Mendeley Data	Mendeley Data: https://doi.org/10.17632/p9hwtxtnfy.1
Digital embryo zebrafish wild-type wt5	CNRS-BioEmergences, this paper, Mendeley Data	Mendeley Data: https://doi.org/10.17632/dw7jxg972b.1
Digital embryo zebrafish wild-type + gsc wt6	CNRS-BioEmergences, this paper, Mendeley Data	Mendeley Data: https://doi.org/10.17632/58rz299z74.1
Digital embryo zebrafish oep mutant oep1	CNRS-BioEmergences, this paper, Mendeley Data	Mendeley Data: https://doi.org/10.17632/kgpvj9cjx7.1
Digital embryo zebrafish oep mutant oep2	CNRS-BioEmergences, this paper, Mendeley Data	Mendeley Data: https://doi.org/10.17632/scrz9jk7m6.1
Digital embryo zebrafish oep mutant oep3	CNRS-BioEmergences, this paper, Mendeley Data	Mendeley Data: https://doi.org/10.17632/h86nxkk6kt.1
Digital embryo zebrafish oep mutant oep4	CNRS-BioEmergences, this paper, Mendeley Data	Mendeley Data: https://doi.org/10.17632/3xd7kph25v.1
Digital embryo zebrafish oep mutant oep5	CNRS-BioEmergences, this paper, Mendeley Data	Mendeley Data: https://doi.org/10.17632/7g9vgm5jg7.1
Software and algorithms		
EmbryoKinematicsFramework	This paper	https://doi.org/10.5281/zenodo.14698253

EXPERIMENTAL MODEL AND SUBJECT DETAILS

Wild-type or *oep*$^{tz57/tz57}$ mutant *Danio rerio* (zebrafish) embryos (Table 1) were stained by RNA injection at the one-cell stage with 100pg H2B-mCherry and 100pg eGFP-HRAS mRNA (Figure S1) prepared from PCS2+ constructs.[53,54] *Tg(-4gsc:EGP)* embryos were counterstained with H2B-mCherry. Embryos raised at 28.5°C for the next 3 h were dechorionated and mounted in a 3-cm Petri dish filled with embryo medium. To position the embryo, the Petri dish had a glass coverslip bottom, sealing a 0.5-mm hole at the dish center, holding a Teflon tore (ALPHAnov) with a hole of 780 μm. The embryo was maintained and properly oriented by infiltrating around it 0.5% low-melting-point agarose (Sigma) in embryo medium.[55] Temperature in the Petri dish differed slightly amongst the specimens depending on the temperature control means (either room temperature control or OKOLAB system, see Table 1). After the imaging procedure, the embryo morphology was checked under the dissecting binocular and the animal was raised for at least 24 h to assess morphological defects and survival. The different datasets encompassed the same developmental period (4–6 hpf to 14–16 hpf). All the specimens were imaged from the animal pole and the imaged volume encompassed the forebrain with some differences depending on the animal positioning in its mold. Variability in the development speed reflects temperature differences as well as intrinsic variability of embryonic development. Regarding gender, embryos were imaged at a very early stage. Also, the mechanisms through which zebrafish determine their sex have come under extensive investigation, as they lack a definite sex-determining chromosome and appear to have a highly complex method of sex determination. Thus, Zebrafish gender is not genetically determined and it depends on environmental conditions. For this reason, the gender was not determined.

We used for this work an available transgenic zebrafish line that carries a gene construct for the expression of a fluorescent protein. Expression of fluorescent reporters in fish does not have adverse effects on development or well-being. The zebrafish line *zoep*$^{tz57+}$ carrying a mutation was maintained as heterozygotes. In this way possible effects of the mutation on the adult phenotype was avoided and homozygous mutant embryos for experiments were obtained from heterozygous parents. The laboratory (CNRS

USR3695) has all the required permits to house and work with transgenic and mutant zebrafish lines. All work with zebrafish strictly followed the EU Animal Protection Directive (2010/63/EU), the European Convention for the protection of vertebrate animals used for experimental and other scientific purposes (Strasbourg, 18th day of March 1986), and national and local legislation. The personnel involved in the fish husbandry were specifically trained for these issues. The fish facility complied with all national and European laws and regulations relating to the transport, housing and use of fish in research and the fish populations were maintained in approved tanks. The facility has annual registration of all zebrafish bred and used in experiments. Access to the fish facility is restricted to qualified personnel that received appropriate training in fish handling and experimentation. Certified veterinarians regularly monitor the sanitary status of the facility and the health status of the fish kept and responsible for overseeing that all regulations are met and that all necessary provisions are taken on animal welfare. All experimental procedures, the sacrifice of fish embryos after experiments, and the disposure of sacrificed fish, was carried out in compliance with all national and European law and regulations. All the work reported here was performed with embryos before hatching that are not subjected to restrictions, thus how protocols were readily approved by the ethics committee.

METHOD DETAILS

In-vivo imaging

Imaging was performed as described[36] with 2-photon laser scanning[56] on Leica SP5 upright microscopes and high numerical aperture 20× water dipping lens objectives. Image acquisition parameters are summarized in Table 1.

The 4D (3D, time-resolved) datasets featured a constant time step Δt of approximately 2.5 min, defining a discrete timescale for the cohort and a voxel size between 1.2 and 1.4 μm^3 (Table S1). Since this time interval is much shorter than the timescale of the gastrulation, we assume instantaneous observations, therefore $\Delta t \sim \delta t$. Digital cell lineages (Figure 1; Figure S1) were obtained through the BioEmergences automated image processing workflow.[36] Cell positions were given by the approximate nucleus centers after applying the nuclei segmentation module of the workflow. The cell lineage data including cell positions at each time step, linkage from one time step to the other and linkage between mother and daughter cells at the time of cell division was computed by the cell tracking module and presented in a comma-separated-values (.csv) table format (cell identifier and position, mother identifier called as such whether the cell divides or not). As reported in Faure et al.,[36] based on manual annotations and corrections made through the tool Mov-IT, the BioEmergences tracking method yielded an error rate of approximately 2% representing the percentage of false or missing links between two consecutive time steps $[t, t+\delta t]$.

Flow field approximation of cell lineage

We used the cell lineage to provide a complete, structured, spatiotemporal information about cell trajectories, including cell divisions. Specifically, we proposed a generalized data record for each cell nucleus within the lineage as follows:

$$\{cellid,\ motherid, x, y, z, t\}_i$$

where *i* indexes the detected cells (a new *i* is created at each mitosis and allocated to one of the daughter cells), *cellid* is the unique identifier of the local node representing cell *i* at the (x, y, z, t) spatiotemporal nucleus position in the lineage tree, and *motherid* is the identifier of the linked nucleus position at the previous time step (mother cell). The set of detected nuclei form a discrete spatiotemporal map.

Gaussian filtering of tVhe velocity field with temporal information

Given a temporal resolution of the time-lapse data of $\delta t \sim 2.5$ min, singular cell displacements produced by divisions or tracking errors occurred at a frequency close to the sampling's Nyquist frequency and were thus assumed to generate high-frequency noise. To filter out this noise, we performed a temporal smoothing of the displacements along the cell lineage with a Gaussian kernel $N(0, T)$, where T is a timescale in the order of several minutes. By testing several parameters, we set $T = 10$ min to modify the samples of the original velocity field at x_i and generate a smoothed velocity field $v_T(x_i)$ with the same temporal resolution and spatial distribution. In addition, displacements over the threshold *MaxMov* = 9 $\mu m/\delta t$ were removed as outliers. Overall, this filtering helped remove and smooth out vectors resulting from segmentation and tracking errors.

$$\mathbf{v}_T(\mathbf{x}_i(t)) = \frac{1}{\alpha_{i,R}} \sum_{t' \in \Pi} w_{i,T}(t') \mathbf{v}_T(\mathbf{x}_i(t + t')) \qquad \text{(Equation 1)}$$

$$w_{i,T} = e^{-\frac{t^2}{2T^2}} \text{ if i is well tracked}$$

$$w_{i,T} = 0 \text{ if not}$$

$$\Pi = \{t + k\delta t \mid k \text{ integer } k\delta t \in [-2T, 2T]\}$$

$$\alpha_{i,T}(t) = \sum_{t' \in \Pi} w_{i,T}(t')$$

Regularization of the velocity field with spatial information

The vector field v_T was further filtered around the position of each nucleus x_i through a spatial Gaussian kernel $N(0,R)$ obtaining smoothed versions of the velocity field $v_{TR}(x_i)$ with the same temporal resolution and the same spatial distribution of samples. Through a regularization process based on the Gaussian filtering characterized by the parameter R and a second-order structure function derived from the field, we tested the differentiability of the new vector field $v_{TR}(x_i)$ and adjusted the parameter R to minimally modify the samples velocity field.

The spatial Gaussian filtering was defined as follows:

$$\mathbf{v}_{TR}(\mathbf{x}_i(t)) = \frac{1}{\beta_{i,R}} \sum_{j \in N_R(i)} w_{i,R}(\mathbf{x}_j)\mathbf{v}_T\left(\mathbf{x}_i(t)\right) \quad \text{(Equation 2)}$$

$$w_{i,R} = e^{-\frac{r^2}{2R^2}}$$

$$\beta_{i,T}(t) = \sum_{t' \in N_R} w_{i,R}(\mathbf{x}_j)$$

where $N_R(i) = \{x_j\}$ is the set of neighbors interpolated, $w_{i,R}(x_j)$ is the weight of each neighbor according to the $N(0,R)$ distribution and $\beta_{i,R}$ the sum of all the weights. In order to preserve boundaries within the displacement field, a binary function $S(x_j,x_i)$ was used to discard outlier displacements:

$$N_R(i) = \{j \mid \|x_j - x_i\| \langle 2R, S(x_j,x_i) = 1\} \quad \text{(Equation 3)}$$

where $S(x_j,x_i)$ comprises three thresholds based on data observation: the maximum angle of deviation against the reference ($\pi/2$), a minimum speed ($0.2\ \mu m/min$) and a maximum ratio of speed against the reference ($3v_T(x_i)$).

To calibrate the spatial filtering $N(0,R)$ and impose local differentiability of the velocity field around each sample x_i, we used a second-order structure function. As the initial velocity field, the vector field $v_{TR}(x_i)$ represents a discretely, inhomogeneously sampled field. The differentiability of a random field is directly related to the differentiability of its covariance $Z(l)$ at the origin $l = 0$, where l is the separation between sampling points. Experimentally, from a practical point of view, it is easier to accurately measure the structure function than the covariance, which is why we use the structure function, $S2$. The two functions are related as $Z(l) = Z(0) - S2(l)/2$ so it does not matter from a fundamental point of view which one is used. The classic result is that v is continuous if $S2(l) -> 0$ with $l -> 0$ and that v is differentiable if $S2(l) \sim l^2$ as generally described in CRAMiR and Leadbetter.[57] Structure functions are often used in noisy flow fields (e.g., turbulence) to determine whether the velocity field is smooth ($u(x+l) - u(x) \sim l$) as opposed to Holder continuous ($(u(x+l) - u(x) \sim l)^\alpha$ with $\alpha < 1$) within a certain lengthscale range (l). Thus, to fit our inhomogeneous and sparse field, we quantify the differentiability of this field using a second-order structure function built in terms of the average velocity differences within n concentric rings around each x_i. Local differentiability is therefore observed when the structure function follows a power law with exponent ≥ 2. The structure function is defined as:

$$S2_i[n] = \left\{ \langle \|v_{TR}(x_k) - v_{TR}(x_i)\|^2 \rangle \right\}_{\phi_{n,i}} \quad \text{(Equation 4)}$$

where $n \in [1,10]$ and $\phi_{n,i}$ denotes that we calculated the discretized function $S2_i[n]$ around each position x_i in concentric rings with the same radius d_l, i.e.,

$$\phi_{n,i} = \{k \mid (n-1)d_l < \|x_k - x_i\| \langle nd_l \} \quad \text{(Equation 5)}$$

We determined the regularized vector field v_{TR} and the kernel width R considering the local differentiability of all field samples. To this end, we computed a time-dependent ensemble average of the $S2_i[n]$ function for each ring $S2(n,t) = \langle S2_i[n] \rangle_{\phi'_n}$, where ϕ'_n is the subset of all the rings derived from $\phi_{n,i}$ after removal of outlier rings. We labeled a ring as an outlier when the function $S(x_j,x_i)$ described above for the cells within the ring was negative for the majority of them, indicating largely divergent information in the ring that, if included in the regularization term, could over smooth the field globally. Testing several parameters, an optimal kernel width was found, $R = 20\ \mu m$, that ensured differentiability while minimally worsening the spatial resolution of the displacement field (Figure S2).

Instantaneous deformation descriptors

The differentiability of the vector flow field v_{TR} allowed us to apply principles of continuum mechanics to quantify cell motion and tissue deformation. We calculated the Incremental Deformation Gradient (IDG) tensor field $f(x_i)$ by a numerical method (least squares

error minimization) considering the displacements of the neighboring cells within the volume defined by $2R$. The IDG tensor for the cell i at position x_i^t and time t defines a mapping from the material (i.e., Lagrangian) vector difference dx_i^t onto the vector $dx_i^{t+\Delta t}$:

$$dx_i^{t+\Delta t} = f dx_i^t \quad \text{(Equation 6)}$$

$$x_i^{t+\Delta t} = x_i^t + v_{TR}\left(x_i^t\right)\delta t$$

We obtained flow topology descriptors as Galilean invariants derived from the tensor Incremental Gradient of Displacements $h = f - I$ (Table S2; Figure 1). These invariants are tensor metrics that are independent of the reference frame orientation and velocity. They are therefore suitable for visualizing and comparing complex *3D* flows. The first, second and third principal invariants in *3D* (referred here as invariants) are interpreted as follows. The first invariant of h (P as described in 41) quantifies the compression/expansion rate at the mesoscopic scale, corresponding to an overall decrease/increase of cell size change in the vicinity of each nucleus. The second invariant (Q as described in 41) gives information about deformation, not producing volume changes at the mesoscopic scale, associated with both irrotational and vortical motions. We identified the deformation produced by rotation the discriminant of the deformation tensor (D), which is positive in regions of mesoscopic rotation. Finally, we designed a topology index descriptor τ that takes four different values representing the combinations of the signs of the descriptors P and D (Figure 2; Figures S3–S5): expansion-rotation (green label), expansion-no rotation (blue label), compression-rotation (yellow label) and compression-no rotation (red label).

To further characterize the strain rates, we calculated the symmetric part of the tensor h that stands for the irrotational, incremental strain tensor ε and its principal components. This symmetric tensor generally provides information about shears and changes in volume through its second invariant Q_s. For tissues that may change volume and in order to distinguish between reconfigurations of the tissues (cell intercalation and cell shape changes) and volume changes (cell size), we calculated the deviatoric tensor d that subtracts volume changes from the strain rate. The eigenvectors $\{d_1, d_2, d_3\}$ and second invariant Q_d of this tensor provided information on the tissue distortion associated to collective cell intercalation and cell shape changes (Table S2; Figure 2; Figures S3–S5).

The description of the vortical motion can be complemented with the angular velocity, computed from the skew-symmetric tensor Ω derived from h. The infinitesimal rotation angle $\delta\alpha$ was derived from ω.

Building Lagrangian Kinematic Profiles

We defined a Lagrangian representation of the flow field by approximating the reconstructed cell trajectories by the flow path lines of the regularized vector flow field. Lagrangian analysis of non-compressible ($P = 0$) two-dimensional flows have been successfully applied to discover Lagrangian Coherent Structures in fluid transport.[58,59] Here, we proposed Lagrangian metrics based on the computation of finite-time deformation tensors to unfold the kinematic history along the lineage. Because of cell divisions and incomplete cell trajectories, the reconstructed cell lineage had to be regularized to build a continuous flow description. We interpolated the cell trajectories with the information of the flow field displacements to generate complete trajectories given an interval of time $[t_n, t_m]$ (Video S17). Thus, we generated a bijective spatiotemporal map $Traj_n^m = \{traj_j\}$ suitable to express the dynamics in terms of trajectories (Lagrangian framework) $v_{TR}(traj_j)$ instead of spatial points (Eulerian framework).

We built Lagrangian Kinematic Profiles (LKPs) using the trajectory flow field. LKPs expressed the instantaneous and cumulative kinematics along each trajectory (Figure 3; Figures S6 and S7; Videos S18 and S19). The cumulative activity was computed for each trajectory by setting a temporal reference t_{ini} and by incrementally enlarging the interval of analysis to generate a sequence of FTDG tensors $F^{t_{ini}}(traj_j)$ (varying along the time interval of the trajectory) and their corresponding descriptor fields. The computation of the FTDG tensor and its invariants (Tables S3 and S4) for each interval $[t_{ini}, t]$ is described below.

Computation of FTDG tensors and descriptors

The IDG tensor field was expressed in Lagrangian terms using the trajectory field $f(traj_j)$ or f_j^t. We composed the tensors along each trajectory and the corresponding time interval with the chain rule (forward-projection matrix operation) to generate a Finite Time Deformation Gradient (FTDG):

$$F_j^{[t_{ini},t]}\{traj_j\} = f_j^{t-1}\ldots f_j^{t_{ini}+1} f_j^{t_{ini}} \quad \text{(Equation 7)}$$

The third invariant of the tensor (ΔV as described in 40) characterized the volume change during the time interval. The finite rotation (tensor R) was segregated from elongation (tensor U) through a polar decomposition $F = RU$[42]. The rotation was described with the angle of rotation $\Delta\alpha$ and the axis of rotation (Euler's theorem as described in 40):

$$\Delta\alpha = \left(\frac{tr(R) - 1}{2}\right) \quad \text{(Equation 8)}$$

The strains were obtained with the right Cauchy-Green tensor $C = F^T F$ and the left Cauchy-Green tensor $B = FF^T$ and their principal components. The invariants of these tensors integrated volume changes and shear strains. Therefore, we calculated the isochoric deformation tensor and the corresponding isochoric Cauchy-Green tensors ($\tilde{C}$ and $\tilde{B}$) to identify the distortion along the

trajectories from the volumetric changes:

$$\tilde{F} = J^{-\frac{1}{3}}F \quad \text{(Equation 9)}$$

The first and second invariants of $\tilde{C}$ and $\tilde{B}$ ($\Delta\gamma_1$ and $\Delta\gamma_2$ as described in[37]) represented the tissue shape changes along the time intervals. The descriptor $\Delta\gamma_1$ (MIC1) evolved linearly with the amount of distortion whereas the descriptor $\Delta\gamma_2$ (MIC2) added second-order terms when the distortion had more than one dimension. Thus together, the $\Delta\gamma_1$ and $\Delta\gamma_2$ descriptors characterized the amount and geometry of tissue shape changes (Table S3; Figure 3; Figures S6 and S7). Aliases have been proposed for finite time descriptors as shown in Table S3.

Visualization of descriptor maps and manual selection of cell domains

The BioEmergences custom visualization tool Mov-IT[36] was used to explore the 4D descriptor maps. The maps for the Eulerian descriptors were computed by generating a color map for the IDG tensor values at each nuclear center x_i. For the cumulative LKPs, color maps were built and visualized with the Mov-IT software by assigning values to the closest nuclear center x_i.

Mov-IT was also used to manually select cell domains and propagate the selections along the cell tracking, in order to perform a statistical analysis of the corresponding LKPs. Two different types of cell populations were selected. Expert embryologists selected cell populations at 10–11 hpf within the hypoblast and epiblast layers that were approximately similar in position and cell number between the five specimens of the cohort. These populations were backtracked to identify the corresponding progenitors at the onset of gastrulation (tail bud selection Figure 4; Figure S8, Video S21). We also selected in embryo *wt1* by the onset of gastrulation the largest possible population of cells kept into the imaged volume throughout the whole imaging sequence (shield selection, Figure 5; Figure S9, Videos S22 and S23). This selection was used to categorize the different types of profiles with unsupervised classification.

Categorization of Lagrangian Kinematic Profiles

A trajectory field defined from the shield cell selection (Figure S9) was further characterized by identifying subdomains with similar LKPs $l_j = l_{traj_j}(t)$ (descriptor along the trajectories). The subdomains were identified by generating a distance d_{LKP} distribution between the LKPs (l_j, l_k) of pairs of cells for each descriptor with a cosine metric, selected because it properly weighted both the magnitude of the descriptor and its deviations a long time:

$$d_{LKP} = d_{cos}(l_j, l_k) = 1 - \frac{l_j l_k{}'}{\sqrt{(l_j l_j{}')(l_k l_k{}')}} \quad \text{(Equation 10)}$$

We applied unsupervised *k*-means clustering to classify the trajectories minimizing the variance of the distance distribution, so that trajectories with similar profiles according to the metric were classified together. The behavior of each cluster was defined using the mean of the trajectory profiles a long time, which is considered suitable because the variance was minimized. Several values of the number of clusters *k* were tested (Figures S10–S12), finding that 3 clusters provided a suitable representation of Canonical Lagrangian Kinematic Profiles (CLKPs) reproducible across specimens (Figure 5; Figures S10–S12).

QUANTIFICATION AND STATISTICAL ANALYSIS

Reduced-order models of Lagrangian tissue deformation: Biomechanical domains

We generated a mechanical signature $\zeta_j(\{CLBP\})$ for each trajectory as a binary feature vector based on the corresponding set of CLKPs (Figure 5; Figure S13). Trajectories were then compared using the Euclidean distance between their mechanical signatures and classified into four representative domains using hierarchical clustering.[60] The obtained classification was used to label the nuclei at the onset of gastrulation (t_{ini}), generating Lagrangian Biomechanical Maps (Figure 5; Figures S14–S16). The spatiotemporal evolution of the biomechanical domains was visualized with Mov-IT by propagating the corresponding labels along the cell trajectories (Figure 5; Figures S14–S16, Videos S22, S23, and S24).

Reduced-order models of *gsc* expression: morphogenetic domains

Analogously, *goosecoid* (*gsc*) profiles were computed from vectors sampling the level of *gsc* reporter expression[41] channel along the trajectories (Figure 6). Each vector was computed as the average value of a spatial region around each trajectory point. Thus, the genetic expression was expressed in a Lagrangian representation to be compared with the mechanical profiles. A clustering module with the same configuration used for CLKPs returned the main *gsc* profiles. Figure 6 showed the spatiotemporal distribution of the clustered *gsc* domains in the embryo in comparison with the mechanical domains. Figure S18 shows the average of the Lagrangian descriptors normalized between 0 and 1 over time.

Lagrangian comparison of embryo specimens based on their LKPs

A comparison between specimens was made using the CLKPs of one embryo as the reference specimen (*wt1*). A time-varying similarity score was defined for each trajectory in the compared embryo $\beta^{ref}_{LKP}(t)$. The score $\beta^{ref}_{LKP}(t)$ represented the similarity of the CLKPs

of the compared embryo with the reference CLKPs at each time point along the interval $[t_{ini}, t_{fin}]$. The similarity score was here defined and computed as the distance of each descriptor CLKP*j* to the corresponding CLKPs of the reference. Then, the smallest distance resulting from each $CLKP_i$ was taken as the score.

$$\beta^{ref}_{LKP}(j,t) = \left\{ d\left(CLKP_j(t), CLKP^{ref}_i(t) \right) \right\}$$

An aggregated similarity score $\beta^{ref}_{ave}(t)$ was computed for eeach embryo as the average of the distance of all CLKPs per time step for each descriptor. Thus, the similarity score of each compared embryo to the reference was presented as a time evolving vector that conveys the information about the timing and temporal distribution of the variability of mechanical activity based on the reference. We used the CLKPs of the reference wild-type embryo (*wt1*) to compare two different wild-type embryos and two mutant embryos (Figure S17).

ADDITIONAL RESOURCES

The workflow tools are available upon request or already available at the BioEmergences workflow website.[36]